Multispectral analog-mean-delay fluorescence lifetime imaging combined with optical coherence tomography

HYEONG SOO NAM,[1,4] WOO JAE KANG,[2,4] MIN WOO LEE,[1] JOON WOO SONG,[3] JIN WON KIM,[3,5] WANG-YUHL OH,[2,6] AND HONGKI YOO[1,*]

[1]Department of Biomedical Engineering, Hanyang University, 222 Wangsimni-ro, Seongdong-gu, Seoul 04673, South Korea
[2]Department of Mechanical Engineering, Korea Advanced Institute of Science and Technology, 291 Gwahang-no, Yuseong-gu, Daejeon 34141, South Korea
[3]Cardiovascular Center, Korea University Guro Hospital, 148 Gurodong-ro, Guro-gu, Seoul 08308, South Korea
[4]Equally contributed to this study
[5]kjwmm@korea.ac.kr
[6]woh1@kaist.ac.kr
[*]hyoo@hanyang.ac.kr

Abstract: The pathophysiological progression of chronic diseases, including atherosclerosis and cancer, is closely related to compositional changes in biological tissues containing endogenous fluorophores such as collagen, elastin, and NADH, which exhibit strong autofluorescence under ultraviolet excitation. Fluorescence lifetime imaging (FLIm) provides robust detection of the compositional changes by measuring fluorescence lifetime, which is an inherent property of a fluorophore. In this paper, we present a dual-modality system combining a multispectral analog-mean-delay (AMD) FLIm and a high-speed swept-source optical coherence tomography (OCT) to simultaneously visualize the cross-sectional morphology and biochemical compositional information of a biological tissue. Experiments using standard fluorescent solutions showed that the fluorescence lifetime could be measured with a precision of less than 40 psec using the multispectral AMD-FLIm without averaging. In addition, we performed *ex vivo* imaging on rabbit iliac normal-looking and atherosclerotic specimens to demonstrate the feasibility of the combined FLIm-OCT system for atherosclerosis imaging. We expect that the combined FLIm-OCT will be a promising next-generation imaging technique for diagnosing atherosclerosis and cancer due to the advantages of the proposed label-free high-precision multispectral lifetime measurement.

References and links

1. C. W. Chang, D. Sud, and M. A. Mycek, "Fluorescence lifetime imaging microscopy," Methods Cell Biol. **81**, 495–524 (2007).
2. P. I. Bastiaens and A. Squire, "Fluorescence lifetime imaging microscopy: spatial resolution of biochemical processes in the cell," Trends Cell Biol. **9**(2), 48–52 (1999).
3. J. Siegel, D. S. Elson, S. E. Webb, K. C. Lee, A. Vlandas, G. L. Gambaruto, S. Lévêque-Fort, M. J. Lever, P. J. Tadrous, G. W. Stamp, A. L. Wallace, A. Sandison, T. F. Watson, F. Alvarez, and P. M. French, "Studying biological tissue with fluorescence lifetime imaging: microscopy, endoscopy, and complex decay profiles," Appl. Opt. **42**(16), 2995–3004 (2003).
4. M. Y. Berezin and S. Achilefu, "Fluorescence lifetime measurements and biological imaging," Chem. Rev. **110**(5), 2641–2684 (2010).
5. T. W. Gadella, *FRET and FLIM Techniques* (Elsevier, 2011), Vol. 33.
6. J. R. Lakowicz, H. Szmacinski, K. Nowaczyk, and M. L. Johnson, "Fluorescence lifetime imaging of free and protein-bound NADH," Proc. Natl. Acad. Sci. U.S.A. **89**(4), 1271–1275 (1992).

7. K. Arakawa, K. Isoda, T. Ito, K. Nakajima, T. Shibuya, and F. Ohsuzu, "Fluorescence analysis of biochemical constituents identifies atherosclerotic plaque with a thin fibrous cap," Arterioscler. Thromb. Vasc. Biol. **22**(6), 1002–1007 (2002).
8. L. Marcu and W. S. Grundfest, "Fluorescence Spectroscopy for Staging Atherosclerotic Lesions," in *Handbook of Biomedical Fluorescence* (CRC Press, 2003), p. 397.
9. A. Žukauskas, P. Vitta, N. Kurilčik, S. Juršėnas, and E. Bakienė, "Characterization of biological materials by frequency-domain fluorescence lifetime measurements using ultraviolet light-emitting diodes," Opt. Mater. **30**(5), 800–805 (2008).
10. J. Park, P. Pande, S. Shrestha, F. Clubb, B. E. Applegate, and J. A. Jo, "Biochemical characterization of atherosclerotic plaques by endogenous multispectral fluorescence lifetime imaging microscopy," Atherosclerosis **220**(2), 394–401 (2012).
11. A. C. Croce and G. Bottiroli, "Autofluorescence spectroscopy and imaging: a tool for biomedical research and diagnosis," Eur. J. Histochem. **58**(4), 2461 (2014).
12. L. Marcu, P. M. French, and D. S. Elson, *Fluorescence Lifetime Spectroscopy and Imaging: Principles and Applications in Biomedical Diagnostics* (CRC Press, 2014).
13. J. R. Lakowicz, H. Szmacinski, K. Nowaczyk, and M. L. Johnson, "Fluorescence lifetime imaging of free and protein-bound NADH," Proc. Natl. Acad. Sci. U.S.A. **89**(4), 1271–1275 (1992).
14. Y. Pu, W. Wang, G. Tang, and R. R. Alfano, "Changes of collagen and nicotinamide adenine dinucleotide in human cancerous and normal prostate tissues studied using native fluorescence spectroscopy with selective excitation wavelength," J. Biomed. Opt. **15**(4), 047008 (2010).
15. L. A. Sordillo, Y. Pu, P. P. Sordillo, Y. Budansky, and R. R. Alfano, "Optical spectral fingerprints of tissues from patients with different breast cancer histologies using a novel fluorescence spectroscopic device," Technol. Cancer Res. Treat. **12**(5), 455–461 (2013).
16. L. Marcu, Q. Fang, J. A. Jo, T. Papaioannou, A. Dorafshar, T. Reil, J.-H. Qiao, J. D. Baker, J. A. Freischlag, and M. C. Fishbein, "In vivo detection of macrophages in a rabbit atherosclerotic model by time-resolved laser-induced fluorescence spectroscopy," Atherosclerosis **181**(2), 295–303 (2005).
17. L. Marcu, J. A. Jo, Q. Fang, T. Papaioannou, T. Reil, J.-H. Qiao, J. D. Baker, J. A. Freischlag, and M. C. Fishbein, "Detection of rupture-prone atherosclerotic plaques by time-resolved laser-induced fluorescence spectroscopy," Atherosclerosis **204**(1), 156–164 (2009).
18. J. Phipps, Y. Sun, R. Saroufeem, N. Hatami, M. C. Fishbein, and L. Marcu, "Fluorescence lifetime imaging for the characterization of the biochemical composition of atherosclerotic plaques," J. Biomed. Opt. **16**, 096018 (2011).
19. Y. Sun, N. Hatami, M. Yee, J. Phipps, D. S. Elson, F. Gorin, R. J. Schrot, and L. Marcu, "Fluorescence lifetime imaging microscopy for brain tumor image-guided surgery," J. Biomed. Opt. **15**(5), 056022 (2010).
20. Y. Sun, J. Phipps, D. S. Elson, H. Stoy, S. Tinling, J. Meier, B. Poirier, F. S. Chuang, D. G. Farwell, and L. Marcu, "Fluorescence lifetime imaging microscopy: in vivo application to diagnosis of oral carcinoma," Opt. Lett. **34**(13), 2081–2083 (2009).
21. J. M. Jabbour, S. Cheng, B. H. Malik, R. Cuenca, J. A. Jo, J. Wright, Y.-S. L. Cheng, and K. C. Maitland, "Fluorescence lifetime imaging and reflectance confocal microscopy for multiscale imaging of oral precancer," J. Biomed. Opt. **18**(4), 046012 (2013).
22. N. P. Galletly, J. McGinty, C. Dunsby, F. Teixeira, J. Requejo-Isidro, I. Munro, D. S. Elson, M. A. Neil, A. C. Chu, P. M. French, and G. W. Stamp, "Fluorescence lifetime imaging distinguishes basal cell carcinoma from surrounding uninvolved skin," Br. J. Dermatol. **159**(1), 152–161 (2008).
23. G. K. Hansson, "Inflammation, atherosclerosis, and coronary artery disease," N. Engl. J. Med. **352**(16), 1685–1695 (2005).
24. G. Pasterkamp, H. M. den Ruijter, and P. Libby, "Temporal shifts in clinical presentation and underlying mechanisms of atherosclerotic disease," Nat. Rev. Cardiol. **14**(1), 21–29 (2017).
25. R. Virmani, A. P. Burke, F. D. Kolodgie, and A. Farb, "Vulnerable plaque: the pathology of unstable coronary lesions," J. Interv. Cardiol. **15**(6), 439–446 (2002).
26. A. V. Finn, M. Nakano, J. Narula, F. D. Kolodgie, and R. Virmani, "Concept of vulnerable/unstable plaque," Arterioscler. Thromb. Vasc. Biol. **30**(7), 1282–1292 (2010).
27. G. Finet, J. Ohayon, and G. Rioufol, "Biomechanical interaction between cap thickness, lipid core composition and blood pressure in vulnerable coronary plaque: impact on stability or instability," Coron. Artery Dis. **15**(1), 13–20 (2004).
28. J. Cai, T. S. Hatsukami, M. S. Ferguson, W. S. Kerwin, T. Saam, B. Chu, N. Takaya, N. L. Polissar, and C. Yuan, "In vivo quantitative measurement of intact fibrous cap and lipid-rich necrotic core size in atherosclerotic carotid plaque: comparison of high-resolution, contrast-enhanced magnetic resonance imaging and histology," Circulation **112**(22), 3437–3444 (2005).
29. V. C. Cappendijk, A. G. Kessels, S. Heeneman, K. B. Cleutjens, G. W. H. Schurink, R. J. T. J. Welten, W. H. Mess, R. J. van Suylen, T. Leiner, M. J. Daemen, J. M. van Engelshoven, and M. E. Kooi, "Comparison of lipid-rich necrotic core size in symptomatic and asymptomatic carotid atherosclerotic plaque: Initial results," J. Magn. Reson. Imaging **27**(6), 1356–1361 (2008).
30. H. M. Loree, R. D. Kamm, R. G. Stringfellow, and R. T. Lee, "Effects of fibrous cap thickness on peak circumferential stress in model atherosclerotic vessels," Circ. Res. **71**(4), 850–858 (1992).

31. M. S. Brown and J. L. Goldstein, "Lipoprotein metabolism in the macrophage: implications for cholesterol deposition in atherosclerosis," Annu. Rev. Biochem. **52**(1), 223–261 (1983).
32. J. J. Boyle, "Macrophage activation in atherosclerosis: pathogenesis and pharmacology of plaque rupture," Curr. Vasc. Pharmacol. **3**(1), 63–68 (2005).
33. J. A. Jo, J. Park, P. Pande, S. Shrestha, M. J. Serafino, J. J. Rico Jimenez, F. Clubb, B. Walton, L. M. Buja, J. E. Phipps, M. D. Feldman, J. Adame, and B. E. Applegate, "Simultaneous morphological and biochemical endogenous optical imaging of atherosclerosis," Eur. Heart J. Cardiovasc. Imaging **16**(8), 910–918 (2015).
34. J. Park, J. A. Jo, S. Shrestha, P. Pande, Q. Wan, and B. E. Applegate, "A dual-modality optical coherence tomography and fluorescence lifetime imaging microscopy system for simultaneous morphological and biochemical tissue characterization," Biomed. Opt. Express **1**(1), 186–200 (2010).
35. G. S. Mintz, S. E. Nissen, W. D. Anderson, S. R. Bailey, R. Erbel, P. J. Fitzgerald, F. J. Pinto, K. Rosenfield, R. J. Siegel, E. M. Tuzcu, and P. G. Yock, "American College of Cardiology clinical expert consensus document on standards for acquisition, measurement and reporting of intravascular ultrasound studies (ivus): A report of the american college of cardiology task force on clinical expert consensus documents developed in collaboration with the european society of cardiology endorsed by the society of cardiac angiography and interventions," J. Am. Coll. Cardiol. **37**(5), 1478–1492 (2001).
36. D. Huang, E. A. Swanson, C. P. Lin, J. S. Schuman, W. G. Stinson, W. Chang, M. R. Hee, T. Flotte, K. Gregory, C. A. Puliafito, and et, "Optical coherence tomography," Science **254**(5035), 1178–1181 (1991).
37. J. Bec, H. Xie, D. R. Yankelevich, F. Zhou, Y. Sun, N. Ghata, R. Aldredge, and L. Marcu, "Design, construction, and validation of a rotary multifunctional intravascular diagnostic catheter combining multispectral fluorescence lifetime imaging and intravascular ultrasound," J. Biomed. Opt. **17**(10), 1060121 (2012).
38. D. Ma, J. Bec, D. R. Yankelevich, D. Gorpas, H. Fatakdawala, and L. Marcu, "Rotational multispectral fluorescence lifetime imaging and intravascular ultrasound: bimodal system for intravascular applications," J. Biomed. Opt. **19**(6), 066004 (2014).
39. H. Fatakdawala, D. Gorpas, J. W. Bishop, J. Bec, D. Ma, J. A. Southard, K. B. Margulies, and L. Marcu, "Fluorescence lifetime imaging combined with conventional intravascular ultrasound for enhanced assessment of atherosclerotic plaques: an ex vivo study in human coronary arteries," J. Cardiovasc. Transl. Res. **8**(4), 253–263 (2015).
40. J. Bec, J. E. Phipps, D. Gorpas, D. Ma, H. Fatakdawala, K. B. Margulies, J. A. Southard, and L. Marcu, "In vivo label-free structural and biochemical imaging of coronary arteries using an integrated ultrasound and multispectral fluorescence lifetime catheter system," Sci. Rep. **7**(1), 8960 (2017).
41. S. Shrestha, M. J. Serafino, J. Rico-Jimenez, J. Park, X. Chen, S. Zhaorigetu, B. L. Walton, J. A. Jo, and B. E. Applegate, "Multimodal optical coherence tomography and fluorescence lifetime imaging with interleaved excitation sources for simultaneous endogenous and exogenous fluorescence," Biomed. Opt. Express **7**(9), 3184–3197 (2016).
42. B. E. Sherlock, J. E. Phipps, J. Bec, and L. Marcu, "Simultaneous, label-free, multispectral fluorescence lifetime imaging and optical coherence tomography using a double-clad fiber," Opt. Lett. **42**(19), 3753–3756 (2017).
43. D. O'Connor, *Time-correlated Single Photon Counting* (Academic Press, 2012).
44. P. V. Butte, Q. Fang, J. A. Jo, W. H. Yong, B. K. Pikul, K. L. Black, and L. Marcu, "Intraoperative delineation of primary brain tumors using time-resolved fluorescence spectroscopy," J. Biomed. Opt. **15**(2), 027008 (2010).
45. T. J. Pfefer, D. Y. Paithankar, J. M. Poneros, K. T. Schomacker, and N. S. Nishioka, "Temporally and spectrally resolved fluorescence spectroscopy for the detection of high grade dysplasia in Barrett's esophagus," Lasers Surg. Med. **32**(1), 10–16 (2003).
46. J. McGinty, N. P. Galletly, C. Dunsby, I. Munro, D. S. Elson, J. Requejo-Isidro, P. Cohen, R. Ahmad, A. Forsyth, A. V. Thillainayagam, M. A. Neil, P. M. French, and G. W. Stamp, "Wide-field fluorescence lifetime imaging of cancer," Biomed. Opt. Express **1**(2), 627–640 (2010).
47. A. Leray, F. B. Riquet, E. Richard, C. Spriet, D. Trinel, and L. Héliot, "Optimized protocol of a frequency domain fluorescence lifetime imaging microscope for FRET measurements," Microsc. Res. Tech. **72**(5), 371–379 (2009).
48. D. R. Yankelevich, D. Ma, J. Liu, Y. Sun, Y. Sun, J. Bec, D. S. Elson, and L. Marcu, "Design and evaluation of a device for fast multispectral time-resolved fluorescence spectroscopy and imaging," Rev. Sci. Instrum. **85**(3), 034303 (2014).
49. J. A. Jo, Q. Fang, T. Papaioannou, and L. Marcu, "Fast model-free deconvolution of fluorescence decay for analysis of biological systems," J. Biomed. Opt. **9**(4), 743–752 (2004).
50. Y. Sun, R. Liu, D. S. Elson, C. W. Hollars, J. A. Jo, J. Park, Y. Sun, and L. Marcu, "Simultaneous time- and wavelength-resolved fluorescence spectroscopy for near real-time tissue diagnosis," Opt. Lett. **33**(6), 630–632 (2008).
51. S. Shrestha, B. E. Applegate, J. Park, X. Xiao, P. Pande, and J. A. Jo, "High-speed multispectral fluorescence lifetime imaging implementation for in vivo applications," Opt. Lett. **35**(15), 2558–2560 (2010).
52. S. Moon, Y. Won, and D. Y. Kim, "Analog mean-delay method for high-speed fluorescence lifetime measurement," Opt. Express **17**(4), 2834–2849 (2009).
53. Y. J. Won, S. Moon, W. T. Han, and D. Y. Kim, "Referencing techniques for the analog mean-delay method in fluorescence lifetime imaging," J. Opt. Soc. Am. A **27**(11), 2402–2410 (2010).
54. Y. J. Won, W. T. Han, and D. Y. Kim, "Precision and accuracy of the analog mean-delay method for high-speed fluorescence lifetime measurement," J. Opt. Soc. Am. A **28**(10), 2026–2032 (2011).

55. Y. Won, S. Moon, W. Yang, D. Kim, W. T. Han, and D. Y. Kim, "High-speed confocal fluorescence lifetime imaging microscopy (FLIM) with the analog mean delay (AMD) method," Opt. Express **19**(4), 3396–3405 (2011).

56. J. Ryu, J. Kim, H. Kim, J. H. Jeong, H. J. Lee, H. Yoo, and D. G. Gweon, "High-speed time-resolved laser-scanning microscopy using the line-to-pixel referencing method," Appl. Opt. **55**(32), 9033–9041 (2016).

57. H. S. Cho, S.-J. Jang, K. Kim, A. V. Dan-Chin-Yu, M. Shishkov, B. E. Bouma, and W.-Y. Oh, "High frame-rate intravascular optical frequency-domain imaging in vivo," Biomed. Opt. Express **5**(1), 223–232 (2014).

58. H. Pal, S. Nad, and M. Kumbhakar, "Photophysical properties of coumarin-120: Unusual behavior in nonpolar solvents," J. Chem. Phys. **119**(1), 443–452 (2003).

59. J. R. Lakowicz, *Principles of Fluorescence Spectroscopy,* 2nd ed. (Kluwer Academic Plenum, 1999).

60. D. Magde, G. E. Rojas, and P. G. Seybold, "Solvent dependence of the fluorescence lifetimes of xanthene dyes," Photochem. Photobiol. **70**(5), 737–744 (1999).

61. S. Lee, M. W. Lee, H. S. Cho, J. W. Song, H. S. Nam, D. J. Oh, K. Park, W.-Y. Oh, H. Yoo, and J. W. Kim, "Fully integrated high-speed intravascular optical coherence tomography/near-infrared fluorescence structural/molecular imaging in vivo using a clinically available near-infrared fluorescence-emitting indocyanine green to detect inflamed lipid-rich atheromata in coronary-sized vessels," Circ. Cardiovasc. Interv. **7**(4), 560–569 (2014).

62. G. J. Tearney, E. Regar, T. Akasaka, T. Adriaenssens, P. Barlis, H. G. Bezerra, B. Bouma, N. Bruining, J. M. Cho, S. Chowdhary, M. A. Costa, R. de Silva, J. Dijkstra, C. Di Mario, D. Dudek, E. Falk, M. D. Feldman, P. Fitzgerald, H. M. Garcia-Garcia, N. Gonzalo, J. F. Granada, G. Guagliumi, N. R. Holm, Y. Honda, F. Ikeno, M. Kawasaki, J. Kochman, L. Koltowski, T. Kubo, T. Kume, H. Kyono, C. C. Lam, G. Lamouche, D. P. Lee, M. B. Leon, A. Maehara, O. Manfrini, G. S. Mintz, K. Mizuno, M. A. Morel, S. Nadkarni, H. Okura, H. Otake, A. Pietrasik, F. Prati, L. Räber, M. D. Radu, J. Rieber, M. Riga, A. Rollins, M. Rosenberg, V. Sirbu, P. W. Serruys, K. Shimada, T. Shinke, J. Shite, E. Siegel, S. Sonoda, M. Suter, S. Takarada, A. Tanaka, M. Terashima, T. Thim, S. Uemura, G. J. Ughi, H. M. van Beusekom, A. F. van der Steen, G. A. van Es, G. van Soest, R. Virmani, S. Waxman, N. J. Weissman, and G. Weisz; International Working Group for Intravascular Optical Coherence Tomography (IWG-IVOCT), "Consensus standards for acquisition, measurement, and reporting of intravascular optical coherence tomography studies: a report from the International Working Group for Intravascular Optical Coherence Tomography Standardization and Validation," J. Am. Coll. Cardiol. **59**(12), 1058–1072 (2012).

63. R. E. Shadwick, "Mechanical design in arteries," J. Exp. Biol. **202**(Pt 23), 3305–3313 (1999).

64. G. J. Tearney, H. Yabushita, S. L. Houser, H. T. Aretz, I. K. Jang, K. H. Schlendorf, C. R. Kauffman, M. Shishkov, E. F. Halpern, and B. E. Bouma, "Quantification of macrophage content in atherosclerotic plaques by optical coherence tomography," Circulation **107**(1), 113–119 (2003).

65. A. Alfonso-García, T. D. Smith, R. Datta, T. U. Luu, E. Gratton, E. O. Potma, and W. F. Liu, "Label-free identification of macrophage phenotype by fluorescence lifetime imaging microscopy," J. Biomed. Opt. **21**(4), 046005 (2016).

66. R. Virmani, A. P. Burke, A. Farb, and F. D. Kolodgie, "Pathology of the vulnerable plaque," J. Am. Coll. Cardiol. **47**(8 Suppl), C13–C18 (2006).

67. H. Yoo, J. W. Kim, M. Shishkov, E. Namati, T. Morse, R. Shubochkin, J. R. McCarthy, V. Ntziachristos, B. E. Bouma, F. A. Jaffer, and G. J. Tearney, "Intra-arterial catheter for simultaneous microstructural and molecular imaging in vivo," Nat. Med. **17**(12), 1680–1684 (2011).

68. S. Kim, M. W. Lee, T. S. Kim, J. W. Song, H. S. Nam, H. S. Cho, S. J. Jang, J. Ryu, D. J. Oh, D. G. Gweon, S. H. Park, K. Park, W. Y. Oh, H. Yoo, and J. W. Kim, "Intracoronary dual-modal optical coherence tomography-near-infrared fluorescence structural-molecular imaging with a clinical dose of indocyanine green for the assessment of high-risk plaques and stent-associated inflammation in a beating coronary artery," Eur. Heart J. **37**(37), 2833–2844 (2016).

69. M. D. Zeiler and R. Fergus, "Visualizing and understanding convolutional networks," in *European Conference on Computer Vision* (Springer, 2014), 818–833.

70. G. J. Ughi, T. Adriaenssens, P. Sinnaeve, W. Desmet, and J. D'hooge, "Automated tissue characterization of in vivo atherosclerotic plaques by intravascular optical coherence tomography images," Biomed. Opt. Express **4**(7), 1014–1030 (2013).

1. Introduction

Fluorescence lifetime imaging (FLIm) [1] is a powerful imaging method that generates an image from the contrast in fluorescence lifetime, which is an intrinsic property of a fluorophore. The fluorescence lifetime is defined as the average fluorescence decay time of the fluorophore excited by pulsed light. The quantitative contrast of fluorescence lifetime, which cannot be obtained by fluorescence intensity imaging alone, makes the FLIm technique attractive to many research fields, such as cell biology [2] and tissue optics [3, 4]. In addition, FLIm is capable of visualizing changes in ion concentration, pH, and temperature in the local cellular environments, and it is being used to detect Förster resonance energy transfer (FRET) [5] at the molecular level. FLIm also has the advantage of robustness since fluorescence

lifetime is independently determined regardless of fluorescence intensity, meaning that the technique is less affected by variations in imaging geometry than other intensity-based techniques.

Endogenous fluorophores in biological tissues such as collagen, elastin, nicotinamide adenine dinucleotide (NADH), flavin adenine dinucleotide (FAD), lipoproteins, and fatty acid show strong autofluorescence with different fluorescence emission bands and lifetimes under ultraviolet excitation [6–12]. Upon ultraviolet excitation, collagen and elastin exhibit fluorescence lifetimes of about 4 nsec and 3 nsec with fluorescence emission peaks of 390 nm and 410 nm, respectively [10–12]. NADH exhibits a fluorescence emission peak of 460 nm, but the fluorescence lifetime of NADH changes depending on the binding state of NADH to the mitochondrial shuttle, i.e., 2 to 4 nsec for bound NADH and about 0.4 nsec for free NADH [13]. Lipoproteins and fatty acid generally exhibit fluorescence emission in a red-shift and wide bandwidth with short fluorescence lifetimes of about 2 to 3 nsec at the lower bandwidth (< 420 nm) and fluorescence lifetimes longer than 5 nsec at the higher bandwidth (> 460 nm) [7, 8, 10–12]. Alterations in the composition of these endogenous fluorophores in biological tissues are deeply associated with the pathophysiological progress of fatal diseases including cancer [14, 15] and atherosclerosis [10]. A multispectral FLIm that can provide information about endogenous fluorophores has the ability to characterize changes in composition and the pathophysiological progress in a label-free manner. These advantages have led to several studies on FLIm imaging of atherosclerotic plaques [10, 16–18], brain tumors [19], oral carcinoma [20, 21], and basal cell carcinoma [22]. These studies demonstrated that FLIm showed superior performance in distinguishing compositions in biological tissues with high accuracy, making FLIm a promising diagnostic technique for atherosclerosis and cancer.

Atherosclerosis imaging with FLIm can be particularly useful in detecting rupture-prone high-risk vulnerable plaques. Atherosclerosis is an inflammatory and vascular remodeling process accompanied by the accumulation of lipid-laden macrophages in the intimal layer of a coronary artery [23]. Vulnerable plaques are defined as unstable atherosclerotic plaques that are highly prone to rupture, which can lead to intra-arterial thrombosis and its associated fatal consequences such as myocardial infarction [24]. Vulnerable plaques are generally characterized by several abnormal features [24–26]: an enlarged lipid-rich necrotic core [27–29], a thin fibrous cap with a thickness of <65 μm covering the necrotic core [27, 28, 30], and increased inflammation due to macrophage infiltration [31, 32]. Therefore, the vulnerability of atherosclerotic plaques is closely related to changes in biochemical compositions, which contain the endogenous fluorophores. Previous FLIm imaging studies of atherosclerosis [10, 16–18, 33, 34] have demonstrated the feasibility of FLIm as a method for characterizing the vulnerability of atherosclerotic plaques and have shown the potential to improve the diagnostic accuracy and sensitivity of imaging modalities to detect vulnerable plaques.

Due to the aforementioned advantages of FLIm for atherosclerosis imaging, several studies have been introduced on the combination of FLIm and morphological imaging modalities such as intravascular ultrasound (IVUS) [35] and optical coherence tomography (OCT) [36] to simultaneously provide morphological and biochemical compositional information of atherosclerotic tissue. Bec *et al.* [37] and Ma *et al.* [38] reported the development of a dual-modal intravascular catheter combined with IVUS. The combined FLIm-IVUS catheters have been successfully demonstrated in human coronary artery *ex vivo* [39] and in swine coronary artery *in vivo* [40] by the same group, showing the potential for the comprehensive imaging in coronary intervention. Furthermore, the dual-modality combined FLIm-OCT system has been suggested in a bench-top configuration for higher spatial resolution and faster imaging speed [34, 41]. Recently, Sherlock *et al.* [42] also developed a fiber-based combined FLIm and OCT endoscopic system using a single double-clad fiber, taking this strategy one step closer to clinical translation.

The standard technique for measuring fluorescence lifetime is the time-correlated single photon counting (TCSPC) method [43], which determines the fluorescence lifetime from a histogram of photon arrival time reconstructed from the detection of individual fluorescence photons by a periodic excitation. TCSPC can produce a fluorescence lifetime measurement with high temporal resolution, high accuracy, and good photon economy, but it suffers from very slow measurement speed, which is not suitable for fluorescence lifetime imaging *in vivo*. To overcome the speed limitation, alternative measurement methods such as pulse sampling [44, 45], gating [46], and the phase modulation [47] method have been introduced due to recent advances in fast electronics and detectors. The pulse sampling method directly measures short fluorescence emission pulses using a gated intensified microchannel plate photomultiplier tube (MCP-PMT) with a fast rise time and a narrow time response, an amplifier with a broad bandwidth, and a ultrahigh-speed digitizer [48], then it retrieves a fluorescence exponential decay function from the digitized pulses by a complex deconvolution algorithm [49]. The measurement method has been used in the above-mentioned FLIm studies for atherosclerosis imaging and the FLIm system in the combined system with IVUS or OCT [50, 51]. However, due to detection noise, including Gaussian noise, Poisson noise, and electrical jitter noise, multiple fluorescence decay profiles must be averaged to obtain a high-precision fluorescence lifetime measurement in many studies. This averaging process inevitably decreases the effective measurement speed. Furthermore, the aforementioned method results in inefficiencies in measurement speed because a very low duty cycle (~1%) for gating operation of the MCP-PMT [48] limits the repetition rate of the pulsed laser, decreasing the maximum measurement speed. To translate the FLIm technique into an *in vivo* intravascular catheter-based system for clinical purposes, high-speed and high-precision effective fluorescence lifetime measurement methods are required to reduce cardiac motion artifacts and to minimize the deleterious effects caused by flushing agents from patients.

In this paper, we present a multispectral FLIm under ultraviolet excitation for autofluorescence imaging of fresh biological tissues based on the analog-mean-delay (AMD) method [52–56], a high-speed and high-precision fluorescence lifetime measurement method. Additionally, the multispectral AMD-FLIm subsystem is combined with a custom-built high-speed swept-source OCT subsystem into a dual-modality imaging system that simultaneously visualizes both the depth-resolved morphology and the biochemical compositional information. In the following sections, we describe the theoretical background of the AMD method, Monte Carlo simulations for the multispectral AMD-FLIm, the combined system configuration, methods for performance validation, and experimental results. The developed combined system was validated with fluorescent solutions with known fluorescence lifetimes. *Ex vivo* imaging of atherosclerotic rabbit iliac artery tissue was performed to demonstrate the feasibility of the combined FLIm-OCT system for atherosclerosis imaging.

2. Methods

2.1 The theoretical background of the AMD method

The AMD method [52–56] can measure fluorescence lifetime based on the facts that the mean-delay of a fluorescence exponential decay is mathematically identical to the fluorescence lifetime, where mean-delay is defined as a signal centroid on the time domain, $\int t \cdot i(t)dt / \int i(t)dt$, and that the convolution in the time domain can be transformed as an algebraic sum in the mean-delay domain. Thus, the fluorescence lifetime, τ, is simply determined by subtracting the mean-delay of the instrumental response function (IRF) from that of the measured fluorescence emission pulse as follows:

$$
\begin{aligned}
\tau = MD_{decay} &= MD_{em} - MD_{irf} \\
&= (MD_{ex} + MD_{decay} + MD_{pd}) - (MD_{ex} + MD_{pd}) \\
&= \left(\frac{\int t \cdot i_{em}(t)dt}{\int i_{em}(t)dt} \right) - \left(\frac{\int t \cdot i_{irf}(t)dt}{\int i_{irf}(t)dt} \right)
\end{aligned}
\tag{1}
$$

where MD_{decay}, MD_{em} and MD_{irf} denote the mean-delays of the fluorescence exponential decay function ($i_{decay}(t) = Ae^{-t/\tau}$), the measured fluorescence emission pulse ($i_{em}(t)$), and the IRF ($i_{irf}(t)$), respectively. MD_{em} is equal to the sum of MD_{ex}, MD_{decay}, and MD_{pd}, which are the mean-delays of the excitation light pulse ($i_{ex}(t)$), the fluorescence exponential decay function, and the impulse response ($i_{pd}(t)$), respectively. On the other hand, MD_{irf} is equal to the sum of MD_{ex} and MD_{pd} because the IRF is measured from a reflected light from a substance with a zero fluorescence lifetime. Note that $i_{em}(t)$ is equal to $i_{ex}(t) \otimes i_{decay}(t) \otimes i_{pd}(t)$ and $i_{irf}(t)$ is equal to $i_{ex}(t) \otimes i_{pd}(t)$, where $\otimes$ denotes convolution operation. This simple deconvolution process effectively eliminates the effect of the photodetector response time. Therefore, the AMD-FLIm method can be implemented using a relatively low bandwidth PMT instead of expensive high-speed electronics such as a gated intensified MCP-PMT, a broad-bandwidth amplifier, and a broadband digitizer. While the very low duty cycle for gating operation of the MCP-PMT [48] limits the maximum measurement speed, the measurement speed of the AMD-FLIm can be increased up to the repetition rate of the pulsed laser. Real-time AMD-FLIm has been demonstrated using a femtosecond Ti-Sapphire laser with a repetition rate of 76 MHz [56]. Not only is this method economically advantageous, but it has been demonstrated that the AMD method can measure fluorescence lifetime with high accuracy and photon economy that is as good as that of TCSPC. Accordingly, this promising fluorescence lifetime measurement method could be the best for *in vivo* FLIm applications in terms of both performance and cost.
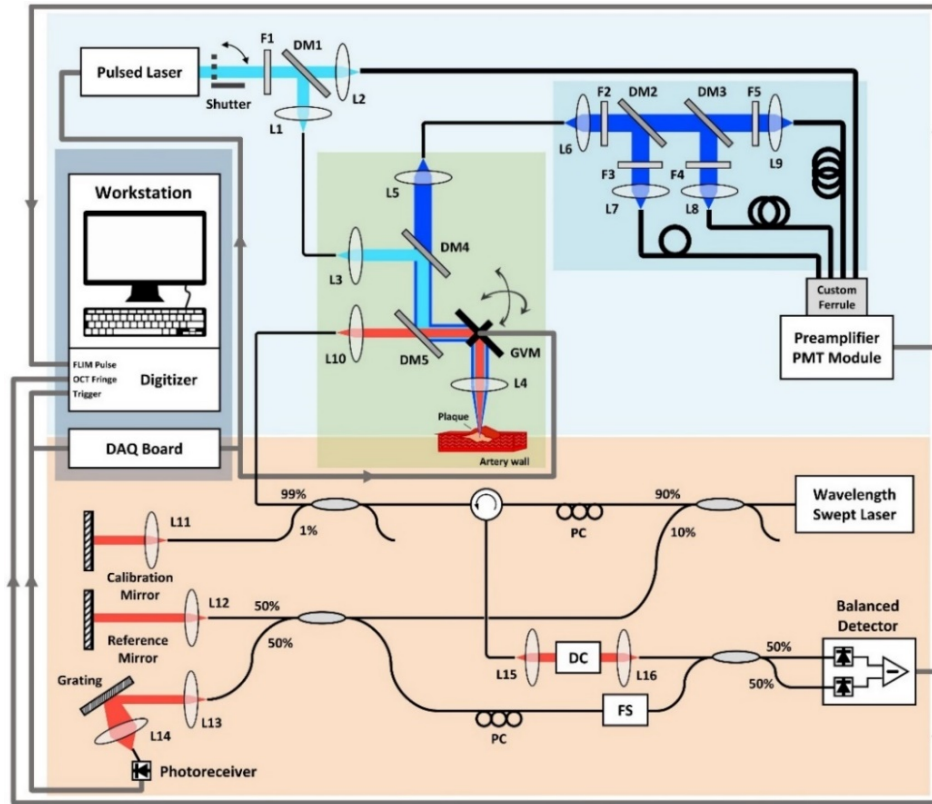
2.2 Combined system configuration

Fig. 1. A schematic diagram of the combined FLIm-OCT system with the OCT subsystem (orange), the FLIm subsystem (sky-blue), the combining optics of FLIm and OCT (green), and the workstation and data acquisition system (navy). Gray and black lines are electronic wires and optical fibers, respectively. DM: dichroic mirror; L: lens; F: filter; GVM: galvano mirror; DC: dispersion compensator; FS: acousto-optic frequency shifter; PC: polarization controller.

Figure 1 shows a schematic diagram of the combined FLIm-OCT system. First, a custom-built high-speed swept-source OCT subsystem [57] is described in the orange-colored portion of Fig. 1. A short cavity wavelength-swept laser was constructed with a fiber-based tunable Fabry-Perot filter (Lambdaquest, CA, USA) and a semiconductor optical amplifier (SOA; BOA1130S, Thorlabs Inc., NJ, USA) with a wavelength sweeping range of 120 nm (centered at 1290 nm), a repetition rate of 120 kHz, and an average output power of 55 mW. The instantaneous linewidth was measured to be 0.15 nm, resulting in a 6-dB roll-off length of 4.5 mm.

The output of the wavelength-swept laser was split at a ratio of 90 to 10, directed to the sample arm and the reference arm, respectively. The reference arm was again split at a ratio of 50 to 50, and one of the halves was directed to a reflective diffraction grating to generate a trigger signal with the same rate as the sweeping repetition rate. The trigger signal was used for external triggering of a two-channel 14-bit digitizer (Signatec PX14400A, DynamicSignals LLC, IL, USA) that simultaneously records an OCT interferogram and a fluorescence emission pulse sequence. To avoid image cross-talk and provide full-depth imaging, an acousto-optics frequency shifter (FS; Brimrose Corp., MD, USA) was added in the reference arm. A dummy AMTIR block was added in the sample arm to compensate for the dispersion by the frequency shifter in the reference arm. The interferogram from a

balanced detector (HCA-S-200M, Femto Messtechnik GmbH, Germany) was recorded on the first channel of the digitizer at a sampling rate of 340 MHz.

A schematic diagram of the multispectral AMD-FLIm subsystem is shown in the sky-blue-colored portion of Fig. 1. A Q-switched diode-pumped solid-state laser (SPOT-10-100-355, Elforlight Ltd., UK) with a 355 nm wavelength, a 1.56 nsec pulse width, a $< \pm 1$ nsec jitter, and a 50 kHz maximum pulse repetition rate was used as the ultraviolet excitation light source. The excitation pulsed laser was triggered by a synchronized trigger signal generated from a data acquisition (DAQ) board (NI-USB-6343, National Instruments, TX, USA). On the DAQ board, one rising edge of the trigger signal for the excitation pulsed laser was generated for every fourth rising edge of the trigger signal for the OCT subsystem. Thus, the excitation pulse train was synchronized, and the repetition rate was one-quarter that of the trigger signal for the OCT subsystem, resulting in a repetition rate of 30 kHz for the excitation pulsed laser in this configuration.

An excitation band-pass filter (F1; ZET355/10x, Chroma Technology Corp., VT, USA) was used to eliminate non-third harmonic components. The light transmitted through the filter was reflected using a dichroic mirror (reflectivity at 355 nm: >98%; DM1; FF376-Di01, Semrock Inc., NY, USA), and it was then coupled to the multi-mode fiber (MMF) with a core diameter of 50 μm (FG050UGA, Thorlabs Inc., NJ, USA). Here, the residual light that was not reflected by the dichroic mirror was used to measure the IRF for every measurement of a fluorescence emission pulse sequence. This simple manipulation enabled the precision enhancement in the fluorescence lifetime measurement by being insensitive to the timing deviation by electrical jitter noises, which can severely degrade the measurement precision in the AMD method, because the common timing deviation by the electrical jitter noises can be cancelled out by itself in the deconvolution process described above [53]. The residual light for the IRF was coupled to the MMF with a core diameter of 400 μm (FVP400440480, Polymicro Technologies LLC, AZ, USA) and a length of 1 m. It was then directed to a photomultiplier tube (PMT; H10720-210, Hamamatsu Photonics, Japan) integrated with a preamplifier module (bandwidth: 50 MHz; Nanoscope Systems Inc., South Korea).

The fluorescence emission from a sample was coupled to the MMF with a core diameter of 200 μm (FG200UEA, Thorlabs Inc., NJ, USA) by an achromatic doublet (L5; PAC15AR.15, Newport Corp., CA, USA). The proposed multispectral AMD-FLIm system has three spectral channels (390/40 nm, 452/45 nm, and 542/50 nm) that are used to simultaneously obtain information on substances with different emission bands and fluorescence lifetimes, such as collagen, elastin, NADH, and lipids. To spectrally and temporally resolve fluorescence emission pulses, we developed a spectral resolving unit (SRU) (the deep sky-blue-colored box in the sky-blue-colored portion of Fig. 1) consisting of a series of dichroic mirrors, optical filters and optical delay-lines with different lengths. In the SRU, the fluorescence emission that passed through a long-pass filter (F2; BLP01-355R-25, Semrock Inc., NY, USA) was spectrally resolved by dichroic mirrors (DM2, DM3; FF414-Di01, FF506-Di03, Semrock Inc., NY, USA) and emission filters (F3, F4, F5; FF01-390/40-25, FF01-452/45-25, FF01-542/50-25, Semrock Inc., NY, USA). Thus, the fluorescence emission was spectrally divided into three wavelength bands of (center wavelength / bandwidth): 390/40 nm (channel 1), 452/45 nm (channel 2), and 542/50 nm (channel 3). The fluorescence emission of each spectral channel was coupled to different MMFs with a core diameter of 400 μm (FVP400440480, Polymicro Technologies LLC, AZ, USA) and lengths of 16, 31, and 46 m, respectively, before being directed to the PMT module. Thereby, the IRF and the fluorescence emission lights of the three spectral channels were temporally resolved with temporal delays of approximately 4.9, 78.2, 151.6, and 224.9 nanoseconds, respectively. In the AMD method, modal dispersion caused by the use of the optical delay lines composed of multimode fibers has little effect on the measured fluorescence emission pulses. The details are provided in the following sections. The spectrally- and temporally-resolved fluorescence

emission pulse sequence detected by the PMT module were recorded on the second channel of the digitizer to be automatically co-registered with the corresponding OCT image.

The combining optics of the FLIm and OCT subsystem and the scanning part are described in the green-colored portion of Fig. 1. The excitation light of the FLIm subsystem was reflected twice by dichroic mirrors with an edge wavelength of 376 nm (DM4; FF376-Di01, Semrock Inc., NY, USA) and 665 nm (DM5; FF665-Di02, Semrock Inc., NY, USA). The light from the OCT subsystem passed through the DM5. Subsequently, the combined lights were scanned by a 2-axis galvanometer mirror scanner (GVM; 6220H, Cambridge Technology Inc., MA, USA), and then focused to the sample through an objective lens (L4; 65595; Edmund Optics Inc., NJ, USA) made of a substrate that can accommodate a wide wavelength band from 350 nm to 1,700 nm (Zeonex E48R, Zeon Corp., Japan). Using the trigger signal of the OCT subsystem as the sample clock, a sawtooth waveform was generated for the fast scan of the 2-axis scanner to set a frame rate of 117 frames per second with 1,024 A-lines and 256 FLIm pixels per frame. The maximum scan range for the fast scan was ± 4 mm, and a step function for the slow scan was generated accordingly to set a maximum field of view of 8 mm by 8 mm. The returning fluorescence emission from the sample was directed to the SRU for spectral-resolving as described above. After passing through the objective, the pulse energy of the FLIm subsystem was 10 nJ. The sensitivity of the OCT subsystem was 99.5 dB, and the axial resolution of the OCT subsystem in air was 11 μm. The transverse resolutions of the FLIm and OCT subsystems were 120 μm and 21 μm, respectively, which were determined from their point spread functions measured using microspheres (InSpeck[TM] Blue 350/440 Microscope Image Intensity Calibration Kit, Thermo Fisher Scientific Inc., MA, USA).

2.3 Monte-Carlo simulation for the multispectral AMD-FLIm

Monte-Carlo simulations were performed to verify that the proposed multispectral AMD method is independent of the modal dispersion caused by the use of the optical delay-lines in the fluorescence lifetime measurement. We assumed that each photon experiences three temporal delays until each photon is detected by a photodetector: (1) the temporal delay when an excitation photon is generated at the laser, (2) the temporal delay while an electron excited by the excitation photon stays in the excited state of the fluorophore, and (3) the temporal delay by modal dispersion of the optical delay-lines composed of multimode fiber. The mean value of the second temporal delay is the fluorescence lifetime by definition. Each temporal delay is determined by different random processes following different probability density functions (PDFs) including: (1) a beta PDF with a positive-skewed shape to emulate an excitation light pulse, (2) an exponential PDF with a rate parameter identical to the reciprocal of a simulated fluorescence lifetime for temporal delay of the excited electron, and (3) the product of the refractive index, length of the optical delay-lines, and the cosine of a random acceptance angle following a Gaussian PDF with a zero mean and a standard deviation of one-half of the maximum acceptance angle determined by the NA of the optical fibers of the delay-lines to model the temporal delay by modal dispersion in the delay-lines. A total of one thousand simulated photons were created to construct a single simulated fluorescence emission pulse, which is the sum of each photon's response delayed by the total temporal delays in the three steps previously described. The impulse response of the photodetector was assumed to be a Gaussian function with a width determined by the bandwidth of the photodetector. Before calculating the mean-delay, the simulated fluorescence emission pulses were digitized and analog-digital converted according to the specifications of the digitizer used for the combined system. The mean-delays were calculated to measure the fluorescence lifetime from the simulated IRF and the simulated fluorescence emission pulse. The simulated IRF was identical to the fluorescence emission pulse with a fluorescence lifetime of 0 nsec. This procedure was repeated 1,000 times to evaluate the accuracy and precision of the fluorescence lifetime measurement.

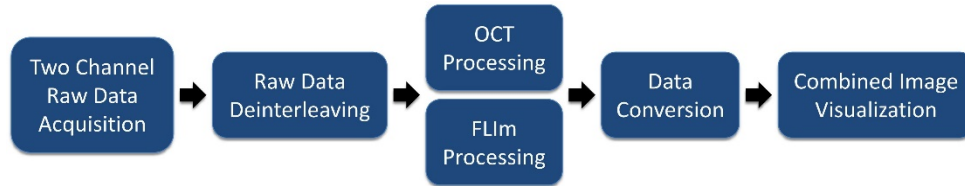## 2.4 Signal and image processing

Fig. 2. Workflow of signal and image processing for the combined FLIm-OCT image visualization, which is split into six steps: two-channel raw data acquisition, raw data deinterleaving, OCT processing, FLIm processing, data conversion, and combined image visualization. Each box represents a task.

The OCT interferograms and the fluorescence emission pulse sequences recorded by the two-channel digitizer were processed based on a multithreading programming technique, and the resulting image was visualized in real-time (Fig. 2).

First, interleaved two-channel raw data from the digitizer were acquired. These data were then deinterleaved to separate the interferograms and the fluorescence emission pulse sequences. Subsequently, the interferograms with 1,024 A-scans were transformed into an OCT image through background removal, k-domain linearization, numerical dispersion compensation, fast Fourier transform, and log conversion for decibel scaling.

At the same time, the fluorescence intensity and lifetime corresponding to the OCT image were calculated from the fluorescence emission pulse sequences. After dc level adjustment and spline interpolation for each pulse of the fluorescence emission pulse sequences, the fluorescence intensity of each spectral channel was calculated by dividing the integral of the fluorescence emission pulse of each spectral channel by that of the IRF pulse. To calculate the fluorescence lifetime from the pulse sequence, the mean-delay of each pulse was determined by an iterative process [52]. (1) The initial mean-delay was set to be the maximum position of each pulse. (2) The initial range of interest (ROI) was set to twice the full-width at half-maximum (FWHM) of each pulse centered at the initial mean-delay so that the fluorescence emission pulse was sufficiently included. If the fluorescence emission pulse is not sufficiently included, the tail side of the pulse that reflects much of the fluorescence exponential decay function cannot be included, resulting in underestimation of the fluorescence lifetime. Thus, we empirically set the width of the ROI to twice the FWHM. (3) The intermediate mean-delay was calculated in the ROI based on the definition of mean-delay in Eq. (1). (4) The intermediate ROI was similar to that in step 2, but was centered at the intermediate mean-delay. (5) Steps 3 and 4 were iterated 10 times, and the final mean-delay of each pulse was obtained. Thereafter, the fluorescence lifetime of each spectral channel was calculated by subtracting the mean-delay of the IRF and the delay-time induced by the optical delay-line for each spectral channel from the mean-delay of the fluorescence emission pulse of each spectral channel.

To effectively visualize the FLIm, the pseudocolor *en face* map was generated based on the HSV (hue, saturation, value) color space, where value and hue represent fluorescence intensity and its lifetime, respectively. After the decibel-scaled OCT image was converted to an 8-bit grayscale image, the pseudocolor information at the corresponding position was superimposed on the bottom of the grayscale OCT image for visualizing co-registered data.

All of the processes were operated on a user-friendly graphical user interface written in C + + based on the Qt Framework (Qt 5.8, The Qt Company, Finland) on a workstation with two Intel Xeon Haswell 8-core E5-2630 v3 @ 2.40 GHz processors and 32 GB of RAM. For the best performance, multithreaded operation functions (e.g., fast Fourier transform, convolution, and matrix operation) that were highly optimized to the Intel CPU provided by Intel Integrated Performance Primitives and the parallel-for loop provided by Intel Threading Building Blocks were used.

2.5 Performance validation and ex vivo imaging

The accuracy and precision of the fluorescence lifetime measurement of the FLIm subsystem were evaluated with various fluorescent solutions with known fluorescence lifetimes including Coumarin 120, POPOP, and Rhodamine 6G (Sigma Aldrich Corp., MO, USA) (Table 1).

Table 1. Fluorescence emission peak and fluorescence lifetime of solutions for performance validation of the FLIm subsystem

Fluorophore	Solvent	Fluorescence emission peak	Fluorescence lifetime
Coumarin 120 [58]	Ethanol	431 nm	3.64 nsec
	Methanol	434 nm	3.85 nsec
	Cyclohexane	380 nm	0.64 nsec
POPOP [59]	Ethanol	410 nm	1.35 nsec
Rhodamine 6G [60]	Ethanol	555 nm	3.99 nsec

To demonstrate the feasibility of using the combined FLIm-OCT system for atherosclerosis imaging, *ex vivo* imaging was performed with iliac specimens from an atherosclerotic rabbit model developed using balloon denudation to their right iliac artery and feeding a high cholesterol diet. A detailed protocol for developing an atherosclerotic rabbit model has been described in a previous publication [61]. The animal experiments were approved by the Institutional Animal Care and Use Committee of Korea University (KOREA-2017-0003) and were performed in accordance with national and institutional guidelines. Within one hour after the experimental rabbit was euthanized, the right atherosclerosis-induced iliac artery and the intact normal artery on the left iliac artery were resected, perfused by saline, cut into pieces of interest, longitudinally opened, placed on a confocal dish, and imaged using the combined FLIm-OCT system. We used two resected iliac specimens for the experiment; one from normal-looking tissue and the other from atherosclerotic tissue. Following imaging, the specimens were embedded in an optimal cutting temperature compound (Sakura Finetek, CA, USA) and frozen at −80 °C. For histopathological analyses, the frozen specimens were sliced to a thickness of 10 μm. Each sliced specimen was stained with hematoxylin and eosin (H&E), Oil-red O (ORO), picrosirius red, or monoclonal mouse anti-rabbit antibody (RAM-11) immunostaining to assess morphology, lipid content, collagen content, and macrophage infiltration, respectively. In addition, we statistically analyzed the fluorescence lifetime distributions of each channel in different regions, which were determined manually compared to the corresponding histopathological sections. The two-tailed unpaired Student's *t*-test was used to determine differences between regions on a pixel-by-pixel basis.

3. Results

3.1 Monte-Carlo simulation for the multispectral AMD-FLIm

The shape parameters of the beta distribution, α and β, were adjusted to 4.5 and 0.345, respectively, for the simulation described in Section 2.3 so that the simulated excitation pulse width was 1.56 nsec, which corresponds to the pulse width of the excitation laser. The bandwidth of the virtual detector was set to 50 MHz, which corresponds to the bandwidth of the PMT-preamplifier module. In addition, we considered the variation in the number of detected photons by shot (Poisson) noise and added white Gaussian noise to the simulated pulse sequence waveform to emulate a practical environment. The simulation was performed for various lengths of optical delay lines for the temporal separation of an IRF and a fluorescence emission pulse.
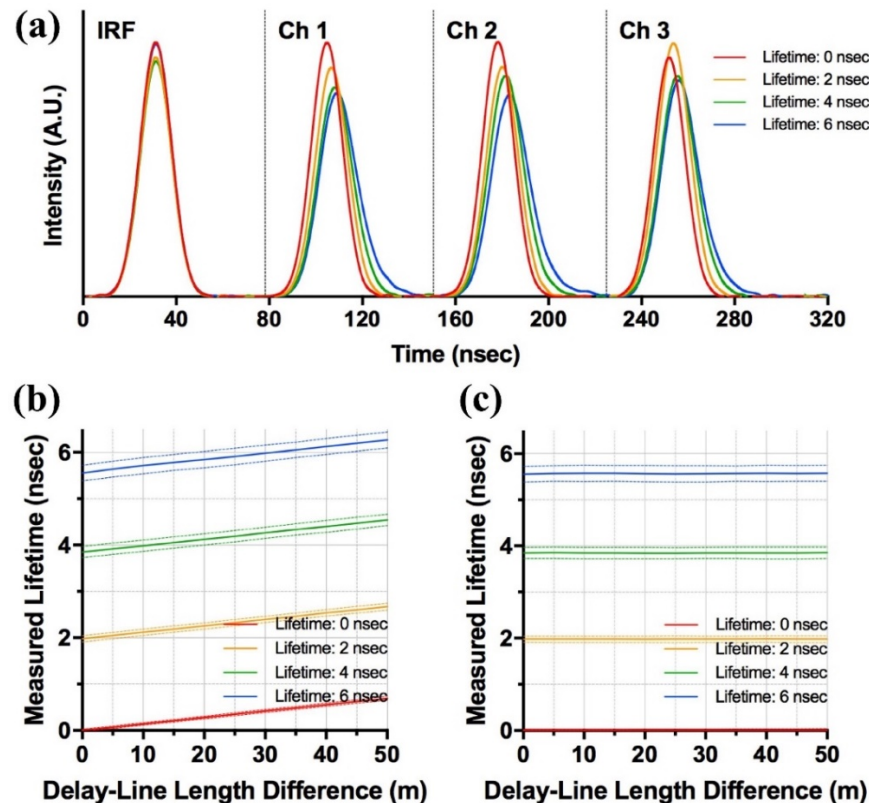
Fig. 3. Monte-Carlo simulation results for the multispectral AMD-FLIm subsystem. (a) Simulated pulse sequence waveforms for the different fluorescence lifetimes (0, 2, 4, 6 nsec) with the optical delay-line lengths of 1 m (IRF), 16 m (Ch 1), 31 m (Ch 2), and 46 m (Ch 3). (b) Results of the simulation for fluorescence lifetime measurements according to the length difference between the two optical delay-lines for the fluorescence emission pulse and the IRF from 0 m to 50 m. (c) Compensation results for the increase in measured fluorescence lifetime due to the use of optical delay-lines. Solid lines and dashed lines in (b) and (c) denote the expected value and the standard deviation (precision) of each simulation with the different fluorescence lifetimes.

Figure 3(a) describes simulated spline-interpolated pulse sequence waveforms with different fluorescence lifetimes of 0, 2, 4, and 6 nsec (red, yellow, green, and blue solid lines in Fig. 3(a), respectively). Each simulated pulse of IRF, channels 1, 2, and 3 was created using the different virtual optical delay lines with lengths of 1 m, 16 m, 31 m, and 46 m, respectively. Note that, since the exponential decay function from the longer fluorescence lifetime has a longer tail, the fluorescence emission pulses with longer fluorescence lifetimes have more asymmetric shapes and longer tails than those with shorter fluorescence lifetimes.

Figure 3(b) shows the simulation results of fluorescence lifetime measurements for the length differences (from 0 to 50 m) of the virtual optical delay-lines between fluorescence emission and IRF, when the length of the virtual optical delay-line for IRF is 1 m. As shown in Fig. 3(b), the measured fluorescence lifetime increases linearly with the length difference of the optical delay-lines due to the modal dispersion of the optical fibers. The slope of all curves was equally measured to be 0.014 nsec/m. Therefore, the increase in measured fluorescence lifetime due to the use of optical delay-lines can be compensated for in a simple manner by subtracting the result of the zero fluorescence lifetime (the red straight-line in Fig. 3(b)) (Fig. 3(c)). In practice, the compensation can be achieved based on the measurement of the fluorescence lifetime of a solution with a known fluorescence lifetime using the three optical delay-lines with the lengths of 16 m, 31 m, and 46 m for each spectral channel.

As shown in Fig. 3(c), the fluorescence lifetime tends to be slightly under-measured for all the simulated fluorescence emission pulses with the different fluorescence lifetimes, especially for pulses with longer fluorescence lifetimes. This is because the ROI is not large enough to fully contain the tail of the fluorescence emission pulse. In other words, the tail of the fluorescence emission pulse reflects more of the exponential decay function than the center of the fluorescence emission pulse. However, since the range of interest of the fluorescence lifetime in this study is below about 5 nsec, which corresponds to a fluorescence lifetime of lipoproteins on the higher bandwidth of >460 nm, the under-measurement tendency does not significantly affect the measurement. Although this underestimation can be readily compensated for, since the relationship between the simulated fluorescence lifetime and the measured fluorescence lifetime is bijective, no compensation for this under-measurement tendency was applied for the following results.

3.2 Performance validation for the multispectral AMD-FLIm subsystem

The fluorescence lifetime of the solutions in Table 1 was measured to evaluate the performance of the FLIm subsystem and to experimentally demonstrate the precision enhancement by the proposed method. Visualization 1 shows the fluorescence emission pulse sequences in practice. Prior to the performance validation, the compensation that involves the measurement and elimination of the additional delay times induced by optical delay-lines was performed using two solutions (POPOP with ethanol and Coumarin 120 with ethanol). This calibration process for the compensation is only required once for the very first imaging. The fluorescence lifetime was measured for each solution for one second (approximately 30,000 times). Table 2 summarizes the results of the fluorescence lifetime measurement for the solutions. For all solutions, the FLIm subsystem can measure fluorescence lifetime with good correspondence to the literature and with a precision within 40 psec without any averaging steps. There are slight differences from the literature, probably because the fluorescence lifetime is sensitive to the external environment including temperature and concentration.

Table 2. Results of fluorescence lifetime measurements for the solutions with known fluorescence lifetimes

Fluorescence solution	Literature lifetime	Measured fluorescence lifetime		
		Ch 1 (390 nm)	Ch 2 (452 nm)	Ch 3 (542 nm)
Coumarin 120 with ethanol[a]	3.64 nsec	3.45 ± 0.03 nsec	3.59 ± 0.04 nsec	-
Coumarin 120 with methanol	3.85 nsec	3.63 ± 0.03 nsec	3.75 ± 0.04 nsec	-
Coumarin 120 with cyclohexane	0.64 nsec	0.82 ± 0.02 nsec	0.97 ± 0.03 nsec	-
POPOP with ethanol[a]	1.35 nsec	1.43 ± 0.03 nsec	1.35 ± 0.03 nsec	-
Rhodamine 6G with ethanol	3.99 nsec	-	-	3.84 ± 0.04 nsec

[a]Solution used to compensate for the delay times by optical delay-lines.

[b]Mean ± standard deviation of the fluorescence lifetime measurement.

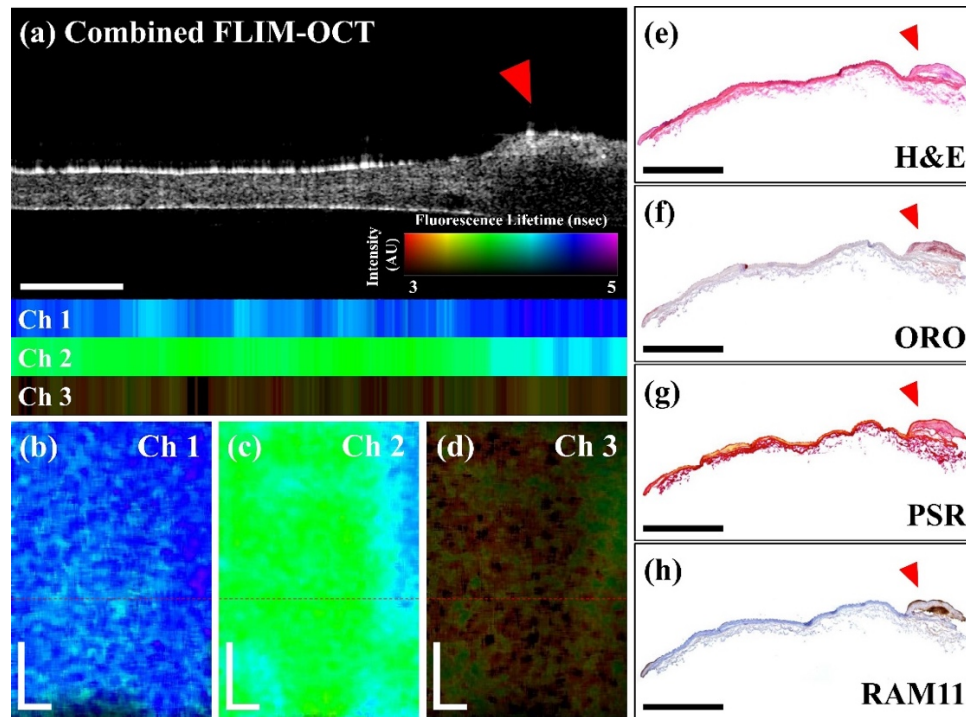### 3.3 Imaging of rabbit iliac arteries ex vivo

Fig. 4. A combined FLIm-OCT imaging result for a normal-looking rabbit iliac artery tissue specimen. (a) An OCT image of the normal-looking specimen combined with the co-registered fluorescence lifetime distribution of the three spectral channels. (b-d) Pseudocolor *en face* maps of fluorescence lifetime distribution of channels (b) 1, (c) 2, and (d) 3, which are represented in HSV color space. Each red dashed line indicates the corresponding position to the image in (a). (e-h) The corresponding histopathological sections: (e) H&E staining, (f) ORO staining, (g) PSR staining, and (h) RAM11 immunostaining. Red arrowheads in (a) and (e-h) show the exact match between the combined FLIm-OCT image and the histological sections. Scale bars are 1 mm.

We performed combined FLIm-OCT imaging for normal-looking and atherosclerotic tissue specimens from a rabbit model with the atherosclerosis-induced iliac artery. Figure 4 shows the imaging results for the normal-looking iliac specimen. The field of view was 6 mm by 6 mm with an acquisition time of about 2.5 sec. As shown in Fig. 4(a), a representative cross-section of the OCT image clearly visualizes thin, flat, and typical of the morphology of a normal artery [62]. The corresponding fluorescence lifetime distribution for the spectral channels is also provided: 4.41 ± 0.06 nsec (Ch 1) and 3.85 ± 0.03 nsec (Ch 2). The resulting fluorescence lifetime distribution is close to that of elastin. This is reasonable because the iliac artery is an elastic artery that contains a large amount of elastin filaments in its tunica media [63]. In addition, the homogenous distribution of the fluorescence lifetime in the *en face* maps (Figs. 4(b-d)) and the corresponding negative and homogenous histopathological sections (Figs. 4(e-h)) suggest that the specimen does not contain neither lipids, collagen, nor macrophages, and that the imaging result is derived from normal arterial tissue with abundant elastin. However, there is a portion showing a different morphology and different fluorescence lifetime distributions of 4.60 ± 0.04 nsec (Ch 1) and 4.19 ± 0.06 nsec (Ch 2) on the right side of the combined image (red arrowhead in Fig. 4(a)). These values represent a statistically significant difference compared to the left side of the combined image, with $p < 0.0001$. The corresponding portion on the histopathological sections (red arrowheads in Figs.

4(e-h)) was also stained positive, revealing that the difference might be due to other tissue components, such as lipids and collagen, and macrophage infiltration.
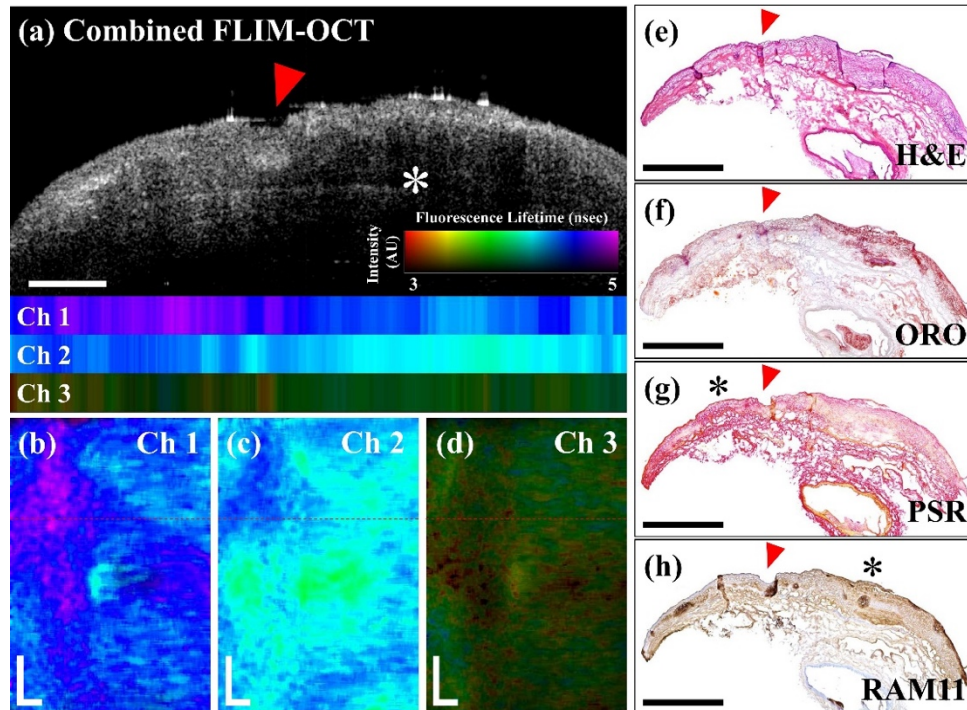

Fig. 5. A combined FLIm-OCT imaging result for an atherosclerotic rabbit iliac artery tissue specimen. (a) An OCT image of the atherosclerotic specimen combined with the co-registered fluorescence lifetime distribution of the three spectral channels. (b-d) Pseudocolor *en face* maps of fluorescence lifetime distribution of channels (b) 1, (c) 2 and (d) 3, which are represented in HSV color space. Each red dashed line indicates the corresponding position to the image in (a). (e-h) The corresponding histopathological sections: (e) H&E staining, (f) ORO staining, (g) PSR staining, and (h) RAM11 immunostaining. Red arrowheads in (a) and (e-h) show the exact match between the combined FLIm-OCT image and the histological sections. Scale bars are 1 mm.

Figure 5 shows the imaging results for the atherosclerotic iliac specimen. The field of view was 8 mm by 6 mm with an acquisition time of about 2.5 sec. As shown in Fig. 5(a), atherosclerotic tissue became thicker, and there was a signal-poor region with a diffusing boundary (white asterisk in Fig. 5(a)) due to the presence of lipid-laden foam cells with a high absorption property [62]. Especially, macrophages appeared to spread over the surface of the tissue and more densely in the signal-poor region because the regions with macrophages were visualized as punctate regions with high attenuation in the OCT images [64]. The results of the atherosclerotic iliac specimen (Figs. 5(b, c)) show statistically significant differences from the results of the normal-looking specimen (Figs. 4(b, c)) in both channels, with $p < 0.0001$. In addition, the fluorescence lifetime distribution is different in the left and right portions with respect to the white dashed line of the combined image: Ch1, 4.73 ± 0.06 nsec (left portion) vs. 4.43 ± 0.07 nsec (right portion), $p < 0.0001$; Ch2, 4.35 ± 0.06 nsec (left portion) vs. 4.20 ± 0.04 nsec (right portion) (Fig. 5(a)). In the left portion, both channels 1 and 2 exhibited a longer fluorescence lifetime than the right portion and the normal-looking specimen, because collagen, which has a long fluorescence lifetime in both channels, is densely distributed on the surface of the left portion, which is thought to be fibrous plaques [62]. Thus, we expected collagen to have a larger contribution to the fluorescence signal. The left portion of the picrosirius-stained section (black asterisk in Fig. 5(g)) was positively and deeply stained,

showing the presence of dense collagen. In the right portion with macrophages and lipid, on the other hand, bound NADH in the macrophages and the degradation of collagen on the cap of the fibroatheroma appeared to decrease the fluorescence lifetime of both channels 1 and 2 compared to the left portion [65]. This analysis of the imaging result can also be supported by the histopathological sections (Fig. 5(e-h)). While the RAM11-immunostained section (Fig. 5(h)) shows the macrophages spread over the tissue, the surface of the right portion was stained much darker showing strong macrophage infiltration on the surface of the right portion (black asterisk in Fig. 5(h)) compared with the surface of the left portion. In addition, the right portion of the picrosirius-stained section was faintly stained (Fig. 5(g)) indicating that there was less collagen or degraded collagen as the fibroatheroma advances.

4. Discussion and conclusions

In this paper, we described the development of a dual-modality system combining a high-speed swept-source OCT and a multispectral FLIm built based upon the AMD method for high-speed and high-precision fluorescence lifetime measurements to obtain an image with both morphological and biochemical information. To the best of our knowledge, the precision-enhanced multispectral FLIm based on the AMD method by using a time-domain multiplexed acquisition technique was first implemented in this study. Since the multispectral fluorescence emission pulses as well as the IRF were acquired with a single PMT, we could accurately and precisely measure multispectral fluorescence lifetime regardless of the modal dispersion caused by the use of optical delay-lines. In particular, the combination of the proposed high-precision multispectral AMD-FLIm and the OCT was implemented using a single two-channel digitizer, enabling efficient simultaneous data acquisition and intrinsic co-registration. In addition, we performed imaging experiments on rabbit iliac artery specimens including normal-looking and atherosclerotic tissue to verify the feasibility of the combined system for atherosclerosis imaging. As shown in Figs. 4 and 5 the combined images clearly visualized different cross-sectional morphologies and fluorescence lifetime distributions according to the pathology of the tissue, thus providing the biochemical compositional information for the tissues. Especially, the corresponding histopathological sections showed that the fluorescence lifetime changes are closely related to the compositional changes, such as collagen density, lipid deposition, and macrophage infiltration. The fluorescence lifetime distribution might result from compositions located on the surface of the tissue since the FLIm subsystem is based on ultraviolet excitation with a penetration depth of around 200 μm [33]. Nevertheless, since thin cap fibroatheroma, a high-risk plaque, has a fibrous cap with a thickness of <65 μm [66], and macrophages are often distributed at the boundary between a fibrous cap and a necrotic core [64], the shallow penetration depth is sufficient for atherosclerosis imaging, especially for evaluating inflamed high-risk plaques.

To extend this technology to preclinical and clinical studies, a rotary joint and a ball-lens catheter using a double-clad fiber are now being developed for *in vivo* combined intravascular FLIm-OCT imaging, especially in a coronary artery of a beating heart, where a high-speed endoscopic imaging is required. We believe that the combined multispectral AMD-FLIm method is most suitable for *in vivo* intravascular coronary imaging when combined with OCT. First of all, the proposed multispectral AMD-FLIm enables the high-speed and high-precision fluorescence lifetime measurements [52, 53], which are the requirements for coronary imaging that favor short imaging time. Secondly, the modal dispersion of the multimode fiber that broadens the fluorescence emission pulses is not a problem in AMD-FLIm method. The Monte Carlo simulation demonstrated that the effect of modal dispersion on the mean-delay is linearly dependent on the length of the optical delay-line and can be simply compensated by measuring the fluorescence lifetimes with the different lengths of the optical delay-lines in practice. This is especially advantageous for fiber-based endoscopic imaging, where the fluorescence emission pulses should pass through the multimode fiber or the inner-clad of the double-clad fiber in the imaging probe, which inevitably causes an additional modal

dispersion. Lastly, in spite of the use of relatively inexpensive, narrow bandwidth, and low-speed electronics, the AMD-FLIm achieves performance comparable to that of the previous FLIm techniques [48, 50, 51]. In addition, the measurement speed of the AMD-FLIm can be significantly and efficiently improved by using a pulsed laser with a higher repetition rate. Due to the previously mentioned advantages, *in vivo* catheter imaging with the combined FLIm-OCT system would be more efficient in terms of speed and performance than conventional FLIm-OCT systems [34, 41]. In addition, this system should easily translate into clinical studies due to its fast acquisition speed (120 frames per second), low energy of excitation pulsed light (10 nJ), inexpensiveness, and no need for an exogenous contrast agent unlike other molecular imaging techniques based on exogenous contrast agents [67, 68]. Especially, the light energy per unit illumination area at the sample is calculated to be 0.09 mJ/cm^2, which is about 40 times lower than the maximum permissible exposure level by the ANSI standard of the FLIm subsystem, 3.52 mJ/cm^2 [38].

Theoretically, the AMD method calculates the fluorescence lifetime, the mean-delay of a fluorescence exponential decaying function, under the assumption that the decay follows a single-exponential decaying function [52], which is seldom the case in biological tissue. In spite of this assumption, because the fluorescence lifetime or mean-delay of a multi-exponential decaying function is determined by the exponents and weights of each exponential decaying function, the proposed AMD-FLIm can sufficiently provide average lifetime changes according to the tissue composition. In addition, since the imaging results of the combined FLIm-OCT include various pieces of information, it is somewhat difficult to analyze atherosclerotic lesions at a glance after imaging. Thus, a method to classify plaque types and to evaluate the risks associated with a plaque using a machine learning algorithm such as a convolutional neural network [69] needs to be developed based on morphological features in OCT images [62, 70] and fluorescence intensities and lifetimes of multiple channels. To develop the classification method, experiments on tissues of various types, including normal tissue, fibrotic, macrophage-rich, and lipid-rich plaques, should be conducted. Meanwhile, we plan to assess and quantify how much the biochemical components, such as collagen, elastin, and macrophages, in each tissue contribute to fluorescence lifetime changes based on a histologic analysis.

In short, the combined FLIm-OCT system in this study will advance our understanding of the pathology of atherosclerosis by providing comprehensive images with morphological and biochemical compositional information in a label-free manner. The proposed combined FLIm-OCT system is a promising next-generation imaging technique for precise evaluation of high-risk plaques prior to a fatal coronary event and for early diagnosis of cancer.

Disclosures

The authors declare that there are no conflicts of interest related to this article.